J Infrared Milli Terahz Waves (2025) 46:55
https://doi.org/10.1007/s10762-025-01067-3

RESEARCH

Rh-doped, InGaAs-based Quantum-Photoconductor with Superior Carrier Mobility-Lifetime Trade-off for THz Time-Domain Spectroscopy

Alexander Dohms[1] · Mykhaylo P. Semtsiv[2] · Tina C. Heßelman[1] · Michael Schulz[3] · Steffen Breuer[1] · Lars Liebermeister[1] · Martin Schell[1,4] · Enrique Castro-Camus[3,5] · Martin Koch[3] · William T. Masselink[2] · Robert B. Kohlhaas[1]

Received: 16 May 2025 / Accepted: 28 June 2025

Abstract

Photoconductive antennas (PCAs) are key elements for the implementation of fiber-coupled terahertz (THz) time-domain spectroscopy (TDS) systems as they provide high infrared-to-THz conversion efficiency. However, their performance is fundamentally limited by the trade-off between carrier mobility and lifetime that is inherent to the photoconducitve material. Here, we present for the first time Rh-doped InGaAs-based quantum photoconductors (QPCs), which overcome this limitation by spatially seperating carrier transport and trapping. With this approach, a sub-picosecond carrier lifetime of 0.75 ps is achieved in combination with very high carrier mobility of 3397 cm^2/Vs, which represents a 1.7 times increase compared to state-of-the-art Rh-doped bulk InGaAs PCAs. In addition, we demonstrate the application of these Rh-doped QPCs as photoconductive receivers in a fiber-coupled THz TDS system, achieving a THz spectral bandwidth of more than 6 THz and a peak dynamic range of up to 100 dB. These results are already competitive with the performance of state-of-the-art devices and show the great potential of QPCs for the next generation of fiber-coupled THz TDS systems.

✉ Alexander Dohms
alexander.dohms@hhi.fraunhofer.de

[1] Fraunhofer Institute for Telecommunications, Heinrich Hertz Institute, Einsteinufer 37, 10587 Berlin, Germany

[2] Department of Physics, Humboldt University Berlin, Newtonstraße 15, 12489 Berlin, Germany

[3] Marburg Center for Quantum Materials and Sustainable Technologies and Department of Physics, Philipps Universität Marburg, Renthof 5, 35032 Marburg, Germany

[4] Institute for Solid State Physics, Technische Universität Berlin, Hardenbergstraße 36, 10623 Berlin, Germany

[5] Centro de Investigaciones en Optica A.C., Loma del Bosque 115, 37150 Leon, Mexico

Published online: 06 August 2025

1 Introduction

Terahertz (THz) time-domain spectroscopy (TDS) has become a well-established technique for non-destructive testing and imaging of dielectric materials, semiconductors and functional coatings, with wide applications in science and industry [1, 2]. State-of-the-art commercial THz systems utilize optical excitation at 1550 nm due to the availability of low-cost and reliable ultrafast fiber laser sources from the telecommunications industry. This allows for the implementation of compact, all fiber-coupled THz TDS systems [3, 4], which offer a high degree of measurement flexibility, ease of use and cost effectiveness, all of which cannot be achieved with free-space THz TDS systems.

Key components of these systems are photoconductive antennas (PCAs), which are used as THz emitter and receiver. PCAs generally consist of a dipole-like antenna geometry formed by metal electrodes that are deposited on a mesa-structured photoconductive layer. In the PCA emitter, optically-excited charge carriers are strongly accelerated by large external bias fields ≥ 40 kV/cm, resulting in a current pulse that lasts less than a picosecond and is the source of the emitted THz pulse [5, 6]. For efficient THz generation, i.e. acceleration of charge carriers, the photoconductive material is, thus, required to have very high carrier mobility > 1000 cm^2/Vs and material resistivity > 1000 Ωcm [7]. In addition, our recent studies indicate that an ultrashort carrier lifetime < 1 ps plays a key role in limiting parasitic currents immediately after THz pulse emission, thereby increasing the breakdown voltage threshold of the PCA emitter significantly [7].

In the PCA receiver, optically excited charge carriers are accelerated by the local electric field of the incident THz pulse, which induces a small net current of few nA to μA. By measuring the current for varying delay times between the gating, infrared pulse and the THz pulse the entire THz pulse is sampled coherently [5]. Here, the most critical requirement is an ultrafast carrier lifetime < 1 ps for the accurate and broadband sampling of the THz pulse electric field [8]. In addition, the signal-to-noise ratio can be significantly improved by choosing a photoconductor with high resistivity to reduce the dark current, and high mobility to increase the THz responsivity of the PCA receiver. Therefore, both the PCA emitter and receiver benefit from an ultrafast carrier lifetime and high material resistivity combined with high carrier mobility.

Over the past decades, many different material systems have been investigated with respect to the aforementioned criteria. For 1550 nm excitation, these include ion-implanted InGaAs [9, 10], low temperature grown (LTG) InGaAs [11, 12] as well as Be-doped LTG-InGaAs/InAlAs superlattices [13–16]. In LTG-InGaAs the excessive incorporation of growth defects at low growth temperatures < 350 °C provides sub-picosecond carrier lifetimes but at the same time significantly reduces the carrier mobility due to carrier-defect scattering. Thus, the performance of LTG-PCAs is fundamentally limited by the trade-off between carrier mobility and lifetime. In recent years, significant improvement in the mobility-lifetime trade-off was demonstrated based on transition-metal (TM) doped InGaAs that is grown at higher growth temperatures > 350 °C, at which high carrier mobility > 1000 cm^2/Vs is maintained [7, 17, 18]. Here, transition metals,

such as Rh and Fe, form deep levels in the middle of the bandgap, which act as ultrafast trapping centers and thereby provide carrier lifetimes as short as 200 fs. At the same time, these deep-level dopants compensate free carriers, which increases the material resistivity to 1000 Ωcm and more. This approach has significantly enhanced the performance of all fiber-coupled THz TDS systems, leading to a very high THz output power of up to 1 mW [7, 19] as well as a record dynamic range of up to 137 dB [7].

Nevertheless, the trade-off between carrier mobility on the one hand and carrier lifetime and material resistivity on the other remains. Therefore, decoupling and separate tunability of these properties is promising to further improve the current generation of photoconductive THz emitters and receivers. To achieve this, Dietz et al. were the first to propose superlattice structures that combine undoped, high-mobility InGaAs layers for carrier excitation and acceleration with high-resistance InAlAs barriers for carrier trapping [20]. Based on this approach, high carrier mobility up to 3000 cm^2/Vs combined with high material resistivity up to 5800 Ωcm was achieved [20]. However, the same authors also showed that carrier trapping in the InAlAs barrier is very slow, resulting in carrier lifetimes in the tens of picosecond range [21]. Another approach by Nandi et al. introduced ErAs monolayers between the high mobility InGaAs layers instead of the InAlAs barrier, which was shown to provide carrier lifetimes as short as 440 fs, but at the cost of rather low mobility values < 1000 cm^2/Vs [22, 23]. Thus, all existing approaches to circumnavigate the carrier mobility-lifetime trade-off in THz PCAs have shown substantial limitations.

In this work, we present photoconductive THz antennas based on a quantum photoconductor (QPC) structure, which provides a significant improvement in the carrier mobility-lifetime trade-off beyond the current state-of-the art. The QPC structure was first reported on by Richter et al. in 2020, who demonstrated adjustable, ultrafast conductivity lifetimes down to 200 fs by localized Fe-doping of the trapping layer [24]. Here, we present for the first time QPC structures doped with Rh, which has shown to be a superior dopant in bulk THz PCAs [18, 25, 26]. For photoconductive THz antennas based on the QPC structure, Rh-doping holds additional potential due to its much lower diffusion coefficient compared to Fe [27], which may allow for stronger confined doping of the trapping layer, i.e. less diffusion into the high mobility layer.

The paper is structured as follows: First, we introduce the QPC structure, its working principle and fabrication by molecular beam epitaxy (MBE) and then investigate the diffusion of Rh- and Fe-dopants within the structure. Subsequently, the carrier dynamics and electronic properties of Rh-doped QPCs are investigated and compared to Fe-doped QPCs as well as bulk Rh-doped PCAs, which represent the current state-of-the-art. Lastly, we demonstrate the THz TDS performance of Rh-doped QPC antennas (QPCAs) as THz receivers in a standard THz TDS system.

2 QPC Sample Structure and Growth

The investigated Rh-doped QPC samples were grown on quarter 2" Fe-doped InP substrates using a gas-source molecular beam epitaxy RIBER compact 21 system. The growth temperatures T_G were varied and measured with a thermocouple to

be between 380 °C and 410 °C, which is considered a good indicator of the actual growth temperature. The sample structure is similar to that described in Ref. [24] and consists of a stepped quantum-well unit that is repeated 33 times to form a multi-quantum-well heterostructure. Figure 1a shows the schematic band diagram of one quantum well. It is made up of three different semiconductor layers that are labeled T, W and B according to their functions as trapping, well and barrier layer. The T-layer consists of a 3 nm thick, Rh-doped $In_{0.75}Ga_{0.25}As$ layer with a bandgap of 0.54 eV. Here, the Rh-cell temperature T_{Rh} is adjusted to 1600 °C – 1650 °C, which should suffice to achieve sub-picosecond carrier lifetime [18]. The T-layer is surrounded by two 18 nm thick $In_{0.53}Ga_{0.47}As$ layers with a bandgap of 0.74 eV, which is compatible with optical excitation at a wavelength of 1550 nm. These layers are nominally undoped, and therefore provide high carrier mobility. The T- and W-layers are embedded within 8 nm thick $In_{0.52}Al_{0.48}As$ layers that effectively act as barriers for charge carriers and terminate the quantum well. Finally, strain compensation for the T-layer is achieved by separating each quantum well with a 1.5 nm thick strain compensating AlAs layer. Table 1 summarizes the growth conditions and measured electronic and optical properties of all samples, next to Fe-doped QPC samples, which were presented in Ref. [24] and will hold as a reference in the following.

The working principle of the QPC structure is as follows: Charge carriers are predominantly generated in the high-mobility W-layer by optically induced h2e2

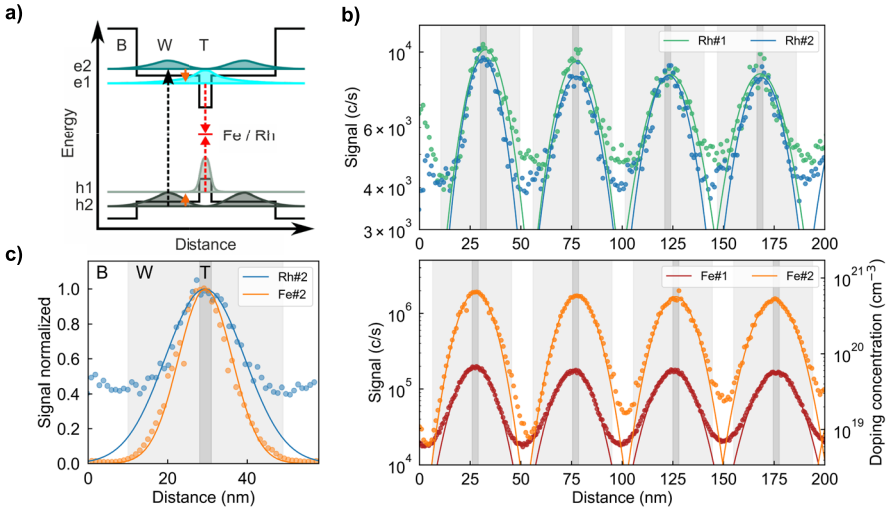

Fig. 1 Comparison of Fe and Rh diffusion in the QPC structure: **a**) Schematic band diagram of a QPC quantum well, consisting of a trapping layer T, a well layer W and a barrier layer B. The probability densities for electron and holes are shown for the subbands e1, e2, h1 and h2. Taken from Ref. [24] and adapted. **b**) Doping profiles in Rh-doped QPC samples (upper graph) next to Fe-doped QPC samples from Ref. [24] (lower graph). Dots are measurement points and lines represent Gaussian fits to the measured data. The average peak FWHM for the Rh-doped samples is 31 nm, compared to 18 nm and 20 nm for the Fe-doped samples Fe#1 and Fe#2. **c**) Comparison of the doping profiles in the first quantum well of sample Rh#2 and Fe#2 showing FWHMs of 23 nm and 16 nm, respectively

interband transition and thereafter relax into the e1 and h1 subbands. The subband separation e2e1 and h2h1 is due to the layer thicknesses and compositions and here adjusted to match the $In_{0.53}Ga_{0.47}As$ longitudinal optical (LO) phonon energy around 33 meV, resulting in very high carrier transition rates into the T-layer [28]. Once confined in the T-layer, i.e. relaxed to the ground state of the QPC, ultrafast carrier trapping occurs via Rh defect states. Thus, in contrast to existing PCA superlattice structures (e.g. [20, 22]), the QPC exploits strong coupling between high mobility carriers and deep level impurities for ultrafast carrier trapping in the T-layer, while the carrier transport in the W-layer should be almost unaffected by the impurities.

However, the QPC working principle, as presented, relies on sharp doping profiles since the diffusion of dopant atoms beyond the trapping layer increases the defect density and thus reduces the carrier mobility in the well layer. To investigate the dopant diffusion, we have measured the doping profiles within the samples Rh#1 and Rh#2 as well as the Fe-doped QPC samples Fe#1 and Fe#2 from Ref. [24] by secondary ion mass spectroscopy (SIMS). Figure 1b shows the depth-resolved SIMS signals for all samples. The background counts were measured to be 18 counts/s (c/s) for the Rh-doped samples and 12 c/s for the Fe-doped samples and are thus negligible compared to the peak signals. The depth resolution was determined to be 5 nm/decade, which implies that a signal change by an order of magnitude requires 5 nm in measurement depth.

The doping profiles in both, the Rh- and Fe-doped QPC samples, show a Gaussian-like distribution centered at the trapping layers, as can be seen by Gaussian fits made to the measured data. We attribute the peak broadening in the doping profiles to diffusion of the dopants beyond the trapping layer, as the peaks are significantly broader than the instrument resolution. For the Rh-doped samples, fitting of all measured quantum wells provides an average FWHM of ~ 31 nm for both samples, compared to 18 nm and 20 nm for the Fe-doped samples Fe#1 and Fe#2, respectively. Thus, against our expectations, the doping profiles indicate slightly lower dopant diffusion in the Fe-doped samples. Nevertheless, a strong doping confinement to the trapping layer can be attributed to all samples as the observed peak broadenings are significantly smaller than the quantum well width of ~ 50 nm. This can also be seen in Fig. 1c, which shows normalized measurements and fits of the first quantum well in the Rh-doped sample Rh#2 next to the Fe-doped sample Fe#2. Here, the FWHM of the fitted peaks are 23 nm and 16 nm, respectively.

Table 1 Sample overview of Rh-doped QPCs including growth conditions, measured Hall mobility μ, carrier concentration N, material resistivity R as well as 1/e carrier lifetime τ_{OPOP} and 1/e conductivity lifetime τ_{OPTP}. Results for Fe-doped QPC samples from Ref. [24] are shown for reference

Sample	T_G (°C)	$T_{Rh/Fe}$ (°C)	μ (cm^2/Vs)	R (Ωcm)	N (cm^{-3})	τ_{OPOP} (ps)	τ_{OPTP} (ps)
Rh#1	380	1650	1699	236	1.56×10^{13}	0.36	0.62
Rh#2	380	1600	2715	351	6.57×10^{12}	0.48	0.76
Rh#3	400	1600	3397	350	5.26×10^{12}	0.75	1.20
Rh#4	410	1600	4515	163	8.46×10^{12}	2.08	-
Fe#1	450	1100	1704	1616	2.27×10^{12}	10.7	-
Fe#2	450	1300	1037	166	3.63×10^{13}	0.38	-

We have determined the absolute iron concentration in the Fe-doped samples by comparing the measurements to a reference sample with known Fe concentration. The Fe concentration averaged over all trapping layers accounts to ~ 6×10^{19} cm^{-3} for the sample Fe#1 with $T_{Fe} = 1100$ °C and to ~ 6×10^{20} cm^{-3} for the sample Fe#2 with $T_{Fe} = 1300$ °C. The absolute Rh concentration in the Rh-doped samples could not be determined by the means of a reference. However, based on the temperature-dependent vapor pressures $p(T_{cell})$ for rhodium and iron effusion cells, as presented in Ref. [18], we estimate that the absolute Rh concentration in the trapping layers at $T_{Rh} = 1600$ °C (equivalent to $p_{Rh} \sim 10^5$ Torr) is similar to the Fe concentration at $T_{Fe} = 1100$ °C ($p_{Fe} \sim 10^5$ Torr) and thus significantly lower than the Fe concentration at $T_{Fe} = 1300$ °C ($p_{Fe} \sim 10^7$ Torr). Thus, despite the slightly larger dopant diffusion observed in the Rh-doped samples, we expect that their W-layers contain a much smaller absolute dopant concentration compared to the Fe-doped sample Fe#2 with $T_{Fe} = 1300$ °C and thus should facilitate higher carrier mobility.

3 Electronic and Dynamic Properties

We have investigated the excited carrier and conductivity lifetimes in our Rh-doped QPC samples using optical-pump optical-probe (OPOP) and optical-pump THz-probe (OPTP) measurements. In both configurations, a femtosecond laser pulse of ~ 90 fs pulse duration and a central wavelength of 1.55 µm was used to excite charge carriers, mainly via the resonant h2e2 interband transition in the well layer of the QPC structure at a pulse fluence of 94 µJ/cm^2 and 130 µJ/cm^2 for the OPTP and OPOP measurement, respectively. In the OPOP measurement, the depopulation of excited states in the e2 and h2 band is determined by measuring the transmission of a probe pulse, which is likewise centered at 1.55 µm, at different times Δt after photo-excitation. For a more detailed description of the measurement setup, the reader is referred to Ref. [17]. Figure 2a shows the logarithmic OPOP signal normalized to the peak transmission value for all samples. Clearly, all traces follow a bi-exponential transmission decay, as indicated by corresponding fits to the measured data. This results from the superposition of two prevailing mechanisms: First, photo-excited charge carriers thermalize and relax into the e1 and h1 subbands, i.e. into the trapping layer, under resonant LO phonon emission, thereby clearing up excited states in the h2 and e2 subbands. Secondly, free charge carriers in the T-layer are trapped in Rh defect states, thus inducing carrier recombination and clearing up the h1 and e1 subbands, which in turn can collect further charge carriers from the h2 and e2 subbands. Based on these mechanisms, the samples Rh#1, Rh#2 and Rh#3 show sub-picosecond 1/e carrier lifetimes of $\tau_{OPOP} = 0.36$ ps, 0.61 ps and 0.75 ps, respectively, while sample Rh#4 shows a slightly larger carrier lifetime of $\tau_{OPOP} = 2.08$ ps.

In the OPTP measurements, a THz TDS system, similar to the one described in Ref. [24], is used to probe the photo-induced conductivity at different times Δt after photo-excitation by measuring the change of transmitted THz pulse amplitude through the sample. Figure 2b shows the logarithmic OPTP signal normalized to the maximum change of transmission of the THz pulse amplitude, which corresponds

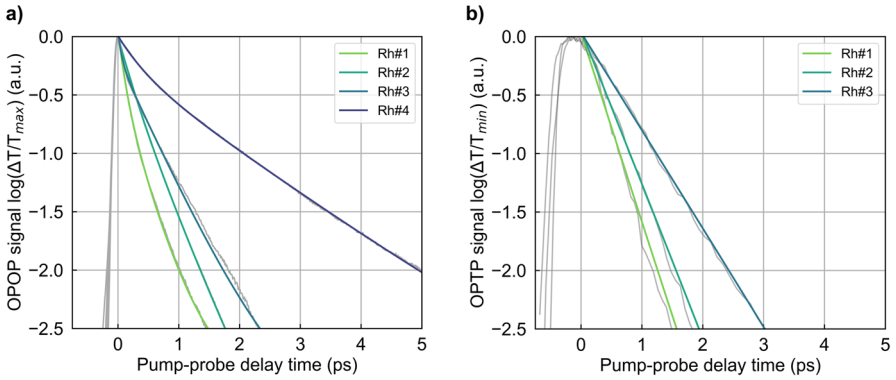

Fig. 2 Carrier and Conductivity lifetime: **a**) OPOP measurements and **b**) OPTP measurements of Rh-doped QPC samples. The measurements are normalized to the maximum transmission value for the optical-probe (OPOP) and minimum transmitted amplitude for the THz-probe (OPTP). The logarithmic signals are fitted using a bi-exponential (OPOP) and mono-exponential (OPTP) fit function

to a pump-probe delay time of $\Delta t = 0$. For all measured samples (Rh#1 to Rh#3), a distinct and relatively broad peak, compared to the OPOP peak, is observed. This is probably due to the longer pulse duration of the THz sampling pulses compared to the optical pulses, which results in a broader instrument response function and, thus, in a lower temporal resolution for the OPTP measurements. The signal peak is followed by a mono-exponential decay of the photoconductivity, which can be related to carrier trapping in the T-layer of the QPC structure. By applying mono-exponential fits to the decays, we obtain 1/e conductivity lifetimes that are slightly longer than those observed by OPOP but with a consistent trend, resulting in values of $\tau_{OPTP} = 0.62$ ps, 0.76 ps and 1.20 ps for the samples Rh#1, Rh#2 and Rh#3, respectively.

In order to investigate the carrier mobility-lifetime trade-off in our samples, Hall effect measurements were conducted in a van der Pauw geometry at room temperature. The results of these measurements, which include the free electron concentration N, the Hall resistivity R and the Hall mobility μ are summarized in Table 1. All investigated samples show remarkably high Hall mobility, ranging from 1699 cm^2/Vs for Rh#1 up to 4515 cm^2/Vs for Rh#4. This indicates a high crystalline quality and comparable low Rh-concentration in the InGaAs well layers of these samples. However, the compensation of free charge carriers by Rh defect states is in turn much lower, when for example compared to homogeneously Rh-doped bulk InGaAs, resulting in relatively high free carrier concentrations of 5.3×10^{12} cm^{-3} to 1.56×10^{13} cm^{-3}. Consequently, the overall resistivity in these samples is found to be comparably low, ranging from only 163 Ωcm to 351 Ωcm.

Figure 3a shows the Hall mobility versus the measured carrier and conductivity lifetimes for our Rh-doped QPC samples next to Rh-doped bulk InGaAs photoconductors (PCs) from Ref. [25], which represent the current state-of-the-art. Clearly, both material systems show a distinct mobility-lifetime trade-off, as the carrier mobility decreases steadily with decreasing carrier lifetime. For the QPC samples,

this trend is due to the different growth conditions of each sample, as shown in Table 1: Rh#1 was grown with a growth temperature of $T_G = 380$ °C and with the highest Rh-cell temperature of $T_{Rh} = 1650$ °C, thus having the highest overall Rh-concentration. This results in the shortest carrier lifetime of 0.36 ps combined with the lowest carrier mobility of 1699 cm^2/Vs. All other samples were grown with a Rh-cell temperature of $T_{Rh} = 1600$ °C, and thus nominally lower Rh-concentration, but at different growth temperatures of $T_G = 380$ °C, 400 °C and 410 °C for the samples Rh#2, Rh3 and Rh#4, respectively. Therefore, sample Rh#2 shows a slightly longer carrier lifetime and higher carrier mobility compared to Rh#1, while the increased growth temperatures for Rh#3 and Rh#4 lead to an overall improvement of the crystalline quality, thereby increasing the carrier mobility and lifetime further.

Figure 3a also shows that Rh-doped QPC samples exhibit significantly higher Hall mobilities than Rh-doped bulk InGaAs PCs. For example, sample Rh#3 achieves a carrier lifetime of 0.75 ps in combination with a very high Hall mobility of 3397 cm^2/Vs, representing a 1.7 times higher Hall mobility in the sub-picosecond regime (Rh-doped PCs: $\tau_{OPOP} \sim 0.95$ ps, $\mu \sim 2000$ cm^2/Vs). This constitutes a significant improvement in the carrier mobility-lifetime trade-off over the current state-of-the-art. If conductivity is considered instead of carrier lifetime, Rh-doped QPCs still provide the overall better trade-off with the carrier mobility. However, in bulk InGaAs PCs the conductivity typically decays instantaneously with the depopulation of the excited states as charge carriers are effectively trapped anywhere in the absorbing layer without the need for a prior transfer to a trapping layer, as it is the case in the QPC structure. Thus, the advantages of the QPC structure in terms of the trade-off between carrier mobility and conductivity lifetime weighs less compared to the carrier mobility-lifetime trade-off.

Compared to Fe-doped QPC samples from Ref. [24] (Fig. 3b), our Rh-doped QPC samples show an even higher improvement for the mobility-lifetime trade-off. We attribute the increase in Hall mobility at comparable carrier lifetime to the enhanced performance of Rh over Fe as ultrafast trapping center for charge carriers. Specifically, the larger atomic radius of Rh should enhance the charge carrier capture cross-section

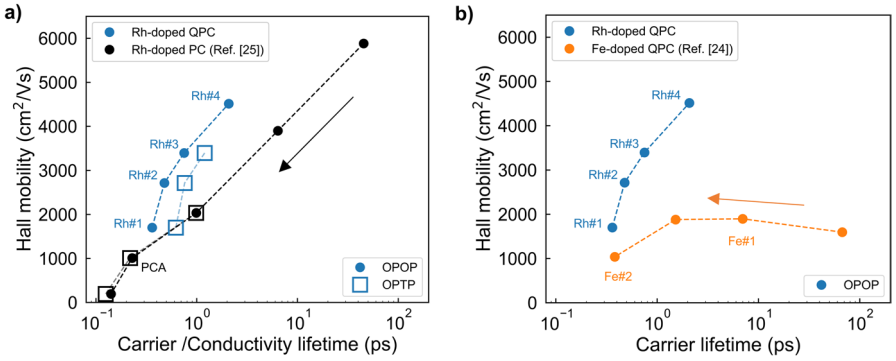

Fig. 3 Hall mobility vs. carrier lifetime (points, measured by OPOP) and conductivity lifetimes (squares, measured by OPTP) in Rh-doped QPC samples. For comparison, measurement data for **a**) Rh-doped bulk InGaAs photoconductor (PC) samples [25] and **b**) Fe-doped QPC samples [24] are shown. Here, arrows indicate the direction of increasing Rh- and Fe-doping concentrations. In **a**) the reference PCA used in section 5 is indicated

compared to Fe and thus lead to sub-picosecond carrier lifetimes at lower doping concentrations, thereby maintaining higher crystal purity. However, at ultrafast carrier lifetime < 400 fs, the difference in Hall mobility between the material systems becomes smaller, indicating a fundamental limit for the mobility-lifetime trade-off in this regime.

4 THz TDS Results

In this section, the performance of our Rh-doped QPCs as THz receivers is tested and compared with state-of-the-art PCAs fabricated from Rh-doped bulk-InGaAs, as presented in Ref. [25] ($\mu = 1000$ cm^2/Vs, $\tau_{OPOP} = 0.23$ ps, R = 3189 Ωcm), and also shown in Fig. 3a. For this purpose, THz receivers were fabricated from sample Rh#4, which combines very high carrier mobility of 4515 cm^2/Vs with moderate carrier lifetime of 2.08 ps. Note that the samples Rh#1 to Rh#3 could not be processed as THz receiver due to the lack of material, which was only enough to either perform OPTP measurements or fabricate THz receiver chips. The fabrication process included a photolithography step for mesa structuring of the multi-quantum well hetero-structure and a subsequent metal sputtering step to implement electrical contacts and a dipole antenna with a 10 µm photoconductive gap. The receiver chips were then separated and packaged as fiber-coupled modules. It should be noted that only THz receiver chips were fabricated and packaged as the measured resistivity of 163 Ωcm for sample Rh#4 was estimated to be too low for the use as THz emitter, which require high electric fields of ≥ 40 kV/cm, i.e. a high electrical breakdown threshold, for efficient THz pulse generation.

All measurements were done using a commercial THz TDS system (TOPTICA TeraFlash pro) with an erbium-doped fiber laser emitting optical pulses with a pulse duration of 90 fs and 1550 nm central wavelength at a repetition rate of 100 MHz. The TDS system employs a fiber-coupled THz emitter based on Fe-doped bulk-InGaAs [17], which is operated at 40 kV/cm bias field and 20 mW optical excitation power. The THz pulses radiated from the emitter were collimated and focused on the receiver module using two off-axis parabolic mirrors. The integration time for all measurements is 60 s.

Figure 4 shows the THz pulse traces and corresponding spectra measured with the Rh-doped QPCA and PCA receivers at 20 mW optical excitation power. The THz spectra are normalized to the noise levels of the receivers, which were taken by blocking the free-space THz path between the emitter and the receiver module. Both receivers show comparable peak-to-peak THz pulse amplitudes of 1241 nA (QPCA) and 1374 nA (PCA), and reach a measurable THz bandwidth of more than 6 THz, while still providing 20 dB of dynamic range (DNR) at this frequency. In addition, both receivers show a similar roll-off, which is linearly decreasing for frequencies > 1 THz. However, their peak DNR differs by 6 dB, as the QPCA receiver only achieves 99 dB at 660 GHz while the PCA reaches up to 105 dB at 1 THz. Moreover, the QPCA performance is much more sensitive to the optical excitation power, as can be seen in the insets of Fig. 4a and b. At low excitation power of 5 mW, the QPCA achieves only 754 nA peak-to-peak amplitude and 94 dB peak DNR compared to 1153 nA and 103 dB for the PCA receiver. For increasing excitation power, the difference in pulse amplitude is compensated, possibly due to the very high carrier mobility in the QPC receiver, which may reduce saturation effects. However, the peak DNR of the QPCA receiver remains lower,

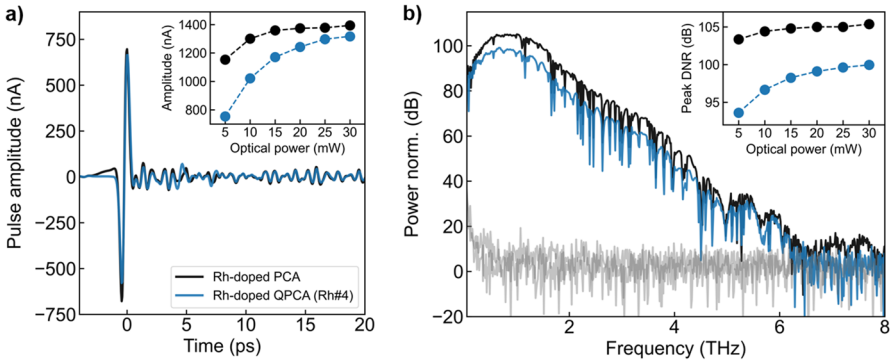

Fig. 4 **a**) Measured THz pulse amplitude and **b**) THz spectra for Rh-doped QPC receivers based on sample Rh#4 and state-of-the-art PCAs based on Rh-doped bulk InGaAs from Ref. [25]. Measurements were taken with a commercial fiber-coupled THz TDS system (Toptica TeraFlash pro) with an integration time of 60 s and 20 mW optical excitation power on the receiver and emitter, respectively. The emitter was biased at 40 kV/cm. The noise spectra were taken with a blocked THz path. Insets show **a**) the pulse amplitude and **b**) the peak dynamic range (DNR) as function of optical excitation power at the receiver

reaching a maximum of 100 dB compared to 106 dB for the PCA. This is possibly due to the longer carrier lifetime of the QPCA, which results in a broadened sampling of the incident THz pulse and increased parasitic currents, and therefore an overall higher noise level. In addition to this, measuring the dark currents of the two THz receivers revealed a 16-times higher dark current for the QPCA compared to the PCA (320 nA and 20 nA, respectively, at 0 V), which may be due to the lower resistivity of the QPCA and is likely to increase its noise. It should be noted that the samples Rh#1 to Rh#3, which have sub-picosecond carrier lifetimes and higher resistivities, may have provided lower noise levels and thus higher peak DNR values.

5 Conclusion

In this work, we report for the first time Rh-doped InGaAs-based quantum photoconductors (QPCs) grown by molecular beam epitaxy at varying growth and Rh-cell temperatures. The doping profile in these multi-quantum-well heterostructures was found to show strong confinement of dopants to the trapping layer, i.e. a low degree of dopant diffusion into the high mobility well layer. As a result, the presented Rh-doped QPC samples combine very high carrier mobility > 1500 cm^2/Vs with very low carrier lifetimes down to 0.36 ps, which facilitates a significant improvement in the carrier mobility-lifetime trade-off over the current state-of-the-art. Furthermore, strong coupling of high mobility carriers with localized defect states, as intended by the QPC structure, was confirmed by OPTP measurements, which showed ultrafast conductivity decay times down to 0.62 ps. In addition, we tested the practical applicability of Rh-doped QPCs by processing THz receiver antennas and utilizing them in a state-of-the-art THz TDS system, achieving a bandwidth of more than 6 THz with a peak dynamic range of up to 100 dB. These results demonstrate that the fabricated QPCA THz receivers are already approaching the performance of state-of-the-art

devices and hold great potential for improving the next generation of fiber-coupled THz TDS systems. In the future, Rh-doped QPCAs may also be optimized for the use as THz emitters, which would require an increase in material resistivity, for example by compensating for the large n-type background in the undoped well layer.

Author Contributions Conceptualization, A.D.; validation, M.P.S., T.C.H., M.S., S.B., L.L., M.S., E.C.C., M.K., W.T.M. and R.B.K.; investigation, A.D.; data curation, A.D.; writing, A.D.; supervision, R.B.K.; funding acquisition, W.T.M., M.K. and R.B.K.; All authors have read and agreed to the published version of the manuscript.

Funding Open Access funding enabled and organized by Projekt DEAL. This research was funded by Deutsche Forschungsgemeinschaft (DFG) (KO1520/11–3, KO 6171/2–3 and MA 1749/24–3). The project on which this publication is based is partly funded by the former German Federal Ministry of Education and Research (today: Federal Ministry of Research, Technology and Space) under the project reference numbers 16FMD01K, 16FMD02 and 16FMD03. ECC would like to acknowledge the support of the Alexander von Humboldt foundation.

Data Availability No datasets were generated or analysed during the current study.

Declarations

Competing interests The authors declare no competing interests.

References

1. P. Jepsen, D. G. Cooke and M. Koch, "Terahertz spectroscopy and imaging – Modern techniques and applications," *Laser & Photonics Reviews,* vol. 5, pp. 124-166, January 2011.
2. M. Naftaly, N. Vieweg and A. Deninger, "Industrial Applications of Terahertz Sensing: State of Play," *Sensors,* vol. 19, p. 4203, September 2019.
3. R. J. B. Dietz, N. Vieweg, T. Puppe, A. Zach, B. Globisch, T. Göbel, P. Leisching and M. Schell, "All fiber-coupled THz-TDS system with kHz measurement rate based on electronically controlled optical sampling," *Optics Letters,* vol. 39, p. 6482, November 2014.
4. M. Yahyapour, A. Jahn, K. Dutzi, T. Puppe, P. Leisching, B. Schmauss, N. Vieweg and A. Deninger, "Fastest Thickness Measurements with a Terahertz Time-Domain System based on Electronically Controlled Optical Sampling," *Applied Sciences,* vol. 9, p. 1283, March 2019.
5. P. U. Jepsen, R. H. Jacobsen and S. R. Keiding, "Generation and detection of terahertz pulses from biased semiconductor antennas," *Journal of the Optical Society of America B,* vol. 13, p. 2424, November 1996.
6. M. Tani, S. Matsuura, K. Sakai and S.-i. Nakashima, "Emission characteristics of photoconductive antennas based on low-temperature-grown GaAs and semi-insulating GaAs," *Applied Optics,* vol. 36, p. 7853, October 1997.
7. A. Dohms, N. Vieweg, S. Breuer, T. Heßelmann, R. Herda, N. Regner, S. Keyvaninia, M. Gruner, L. Liebermeister, M. Schell and R. B. Kohlhaas, "Fiber-Coupled THz TDS System With mW-Level THz Power and up to 137-dB Dynamic Range," *IEEE Transactions on Terahertz Science and Technology,* vol. 14, p. 857–864, November 2024.

8. L. Duvillaret, F. Garet, J.-F. Roux and J.-L. Coutaz, "Analytical modeling and optimization of terahertz time-domain spectroscopy experiments, using photoswitches as antennas," *IEEE Journal of Selected Topics in Quantum Electronics,* vol. 7, p. 615–623, 2001.
9. N. Chimot, J. Mangeney, L. Joulaud, P. Crozat, H. Bernas, K. Blary and J. F. Lampin, "Terahertz radiation from heavy-ion-irradiated In0.53Ga0.47As photoconductive antenna excited at 1.55μm," *Applied Physics Letters,* vol. 87, p. 193510, November 2005.
10. M. Suzuki and M. Tonouchi, "Fe-implanted InGaAs terahertz emitters for 1.56μm wavelength excitation," *Applied Physics Letters,* vol. 86, p. 051104, January 2005.
11. A. Takazato, M. Kamakura, T. Matsui, J. Kitagawa and Y. Kadoya, "Detection of terahertz waves using low-temperature-grown InGaAs with 1.56μm pulse excitation," *Applied Physics Letters,* vol. 90, p. 101119, March 2007.
12. A. Takazato, M. Kamakura, T. Matsui, J. Kitagawa and Y. Kadoya, "Terahertz wave emission and detection using photoconductive antennas made on low-temperature-grown InGaAs with 1.56μm pulse excitation," *Applied Physics Letters,* vol. 91, p. 011102, July 2007.
13. R. Wilk, M. Mikulics, K. Biermann, H. Kunzel, I. Z. Kozma, R. Holzwarth, B. Sartorius, M. Mei and M. Koch, "THz Time-Domain Spectrometer Based on LT-InGaAs Photoconductive Antennas Exited by a 1.55 μm Fibre Laser," in *2007 Conference on Lasers and Electro-Optics (CLEO)*, p. 1-2, 2007.
14. B. Sartorius, H. Roehle, H. Künzel, J. Böttcher, M. Schlak, D. Stanze, H. Venghaus and M. Schell, "All-fiber terahertz time-domain spectrometer operating at 1.5 μm telecom wavelengths," *Optics Express,* vol. 16, p. 9565, June 2008.
15. H. Roehle, R. J. B. Dietz, H. J. Hensel, J. Böttcher, H. Künzel, D. Stanze, M. Schell and B. Sartorius, "Next generation 15 μm terahertz antennas: mesa-structuring of InGaAs/InAlAs photoconductive layers," *Optics Express,* vol. 18, p. 2296, January 2010.
16. I. Kostakis, D. Saeedkia and M. Missous, "Terahertz Generation and Detection Using Low Temperature Grown InGaAs-InAlAs Photoconductive Antennas at 1.55 μm Pulse Excitation," *IEEE Transactions on Terahertz Science and Technology,* vol. 2, p. 617–622, November 2012.
17. B. Globisch, R. J. B. Dietz, R. B. Kohlhaas, T. Göbel, M. Schell, D. Alcer, M. Semtsiv and W. T. Masselink, "Iron doped InGaAs: Competitive THz emitters and detectors fabricated from the same photoconductor," *Journal of Applied Physics,* vol. 121, p. 053102, February 2017.
18. R. B. Kohlhaas, B. Globisch, S. Nellen, L. Liebermeister, M. Schell, P. Richter, M. Koch, M. P. Semtsiv and W. T. Masselink, "Rhodium doped InGaAs: A superior ultrafast photoconductor," *Applied Physics Letters,* vol. 112, p. 102101, March 2018.
19. R. B. Kohlhaas, L. Gingras, E. Dardanis, R. Holzwarth, S. Breuer, M. Schell and B. Globisch, "Fiber-coupled THz TDS system with mW-level THz power," in *2022 47th International Conference on Infrared, Millimeter and Terahertz Waves (IRMMW-THz)*, p. 1-2, 2022.
20. R. J. B. Dietz, M. Gerhard, D. Stanze, M. Koch, B. Sartorius and M. Schell, "THz generation at 1.55 μm excitation: six-fold increase in THz conversion efficiency by separated photoconductive and trapping regions," *Optics Express,* vol. 19, p. 25911, December 2011.
21. R. J. B. Dietz, B. Globisch, M. Gerhard, A. Velauthapillai, D. Stanze, H. Roehle, M. Koch, T. Göbel and M. Schell, "64 μW pulsed terahertz emission from growth optimized InGaAs/InAlAs heterostructures with separated photoconductive and trapping regions," *Applied Physics Letters,* vol. 103, p. 061103, August 2013.
22. U. Nandi, M. Mohammadi, H. Lu, J. Norman, A. C. Gossard, L. Alff and S. Preu, "Material properties and performance of ErAs:In(Al)GaAs photoconductors for 1550 nm laser operation," *Journal of Vacuum Science & Technology A,* vol. 39, p. 023407, February 2021.
23. U. Nandi, M. Scheer, H. Lu, J. C. Norman, A. C. Gossard and S. Preu, "Bias-Dependent Carrier Dynamics and Terahertz Performance of ErAs:In(Al)GaAs Photoconductors," *IEEE Transactions on Terahertz Science and Technology,* vol. 12, p. 353–362, July 2022.
24. P.-H. Richter, E. Kartal, R. B. Kohlhaas, M. P. Semtsiv, M. Schell, W. T. Masselink, B. Globisch and M. Koch, "Ultrafast THz Conductivity Dynamics of a Novel Fe-Doped InGaAs Quantum Photoconductor," *IEEE Transactions on Terahertz Science and Technology,* vol. 10, p. 167–175, March 2020.
25. R. B. Kohlhaas, S. Breuer, S. Nellen, L. Liebermeister, M. Schell, M. P. Semtsiv, W. T. Masselink and B. Globisch, "Photoconductive terahertz detectors with 105 dB peak dynamic range made of rhodium doped InGaAs," *Applied Physics Letters,* vol. 114, p. 221103, June 2019.
26. R. B. Kohlhaas, S. Breuer, L. Liebermeister, S. Nellen, M. Deumer, M. Schell, M. P. Semtsiv, W. T. Masselink and B. Globisch, "637 μW emitted terahertz power from photoconductive antennas based on rhodium doped InGaAs," *Applied Physics Letters,* vol. 117, p. 131105, 2020.

27. A. Näser, A. Dadgar, M. Kuttler, R. Heitz, D. Bimberg, J. Y. Hyeon and H. Schumann, "Thermal stability of the midgap acceptor rhodium in indium phosphide," *Applied Physics Letters,* vol. 67, p. 479–481, July 1995.
28. O. Madelung, W. von der Osten and U. Rössler, Intrinsische Eigenschaften von Elementen der IV. Gruppe und von III-V-, II-VI- und I-VII-Verbindungen, vol. 22a, O. Madelung, Ed., Berlin: Springer-Verlag, 1987.